Efficiency Calibration of the H3D H420 Gamma-Ray Imager

K.P. Ziock,[1] S. Brown,[2] J. Daughhetee,[1] P. Gibbs,[1] D. Goodman,[2] W. Kaye[2], V. Nwadeyi,[3] K. Schmitt[1]

1. Oak Ridge National Laboratory (ORNL), Oak Ridge, TN[1]
2. H3D, Inc., Ann Arbor, MI
3. Savanah River National Laboratory, Aiken, SC

Abstract

The Surplus Plutonium Disposition (SPD) project is down blending tons of Pu for disposal as low-level radioactive waste. The bulk of the work will be performed in three glove box lines currently being developed. Material holdup will be an on-going concern for the operation, and we are exploring the use of gamma-ray imaging as a means of reducing the impact of periodic measurements that would normally require stopping work to collect non-destructive analysis data and the large uncertainties associated with the generalized gamma holdup techniques typically employed. Instead, we plan to permanently install modified versions of the H3D, Inc., H420 gamma-ray imagers (4 per line) to conduct the holdup measurements on an ongoing basis. To determine the amount of Pu present in the gamma-ray images requires careful calibration of the imager response function throughout its field-of-view and across its energy spectrum. To perform the calibration, we are employing techniques developed for comparable calibration of a HPGe imager that now returns holdup values for distributed ^{235}U sources that are good to 3%. The calibration includes using GEANT4 Monte Carlo and detector-response models of the imager. The Monte Carlo codes are used to generate events across the imager's field of view, and the detector-response model is used to distribute the events using a realistic detector resolution kernel. The models are validated by comparing results to calibration data collected in the laboratory. The paper will discuss the status of the models, the accuracy achieved, and various issues associated with the mask and detector designs unique to the H420 instrument.

Introduction

The Surplus Plutonium Disposition (SPD) project seeks to permanently dispose of ~ 40 tons of legacy Pu from the US weapons program by down-blending pure oxide with adulterants and entombing it in the Waste Isolation Pilot Plant geo-repository in New Mexico. The down-blend process will be performed at the Savannah River Site in South Carolina in several glove box lines that are currently under construction [1]. As with any Pu-handling facility, holdup (process material that is retained in the process equipment after all free material is removed) is a concern, and the baseline strategy to determine the amount of holdup is to rely on the Generalized Gamma Holdup (GGH) technique. GGH assays are planned at regular intervals (quarterly), requiring that a glove box line be removed from operation, emptied of all removable material, and then surveyed for residual materials, interrupting operations, and reducing the overall throughput of the facility. GGH is also subject to large systematic uncertainties, currently estimated at ~ 30%, and this is of concern from multiple perspectives, including material control and accountancy, worker dose, and criticality.

The Strategic Laboratory Assessment (SLA) is a joint effort of the Savannah River and Oak Ridge National Laboratories to explore ways to streamline the SPD processes to reduce costs, reduce worker dose, and increase productivity. One of the subtasks in this effort is to explore techniques to improve

holdup determinations [1] and we have arrived at the unique solution of continually monitoring the glove boxes using permanently installed gamma-ray imagers added to some of the light fixtures at the top of the glove box. The light-fixture location was chosen, because as a retrofit, we needed a location that provided a clear view of the glove-box interiors, and lights need these as well. This paper discusses those imagers, and the on-going effort to calibrate their performance at the ^{239}Pu emission lines of interest for SPD (129, 375 and 414 keV), particularly for coded-aperture imaging. A companion paper discusses advanced 3D image reconstruction techniques for the coded-aperture imaging approach used by the instruments [2] while a second [1] provides an overview of the overall imaging approach.

Coded-Aperture Imaging

Coded-Aperture Imaging is a mature technology that allows one to create artifact-free images using gamma-rays emitted by many nuclear materials. It is an indirect-imaging extension of a simple pinhole camera where the single pinhole is replaced by a blocking sheet pierced with many pinholes, allowing more radiation to reach the detector [3]. Originally proposed using random pinhole patterns, it was found that artifacts occurred because the response function to a single point source had pattern-dependent sidelobes that caused source confusion for extended objects and limited the dynamic range of the images. This was solved when specialized patterns that had flat side lobes were reported [4].

The data collected by the detector contains a confusion of many pinhole images and is best thought of as a shadowgram that encodes the scene. The image is reconstructed using cross-correlation analysis with the known mask pattern and the data, where the image, $I_{i,j,}$ in pixel i,j is [4]:

$$I_{i,j} = \sum_{m,n} M_{m-i,n-j} D_{m,n}, \quad (1)$$

where $M_{k,l}$ is the mask function defined to be 1 for open and -1 for closed locations, and $D_{m,n}$ is the counts in detector pixel m,n. The flat side lobes obtained with the advanced patterns arise because the patterns auto-correlate to a delta function, e.g. $I_{i,j} = \delta_{im,jn}$.

Originally developed for gamma-ray astronomy where all sources are in the far field, coded-aperture imaging can easily be adapted to terrestrial use if one takes into account that the mask pattern projected by near-field objects is magnified [5]. In fact, if the source is very close to the imager, then the magnification is a strong function of distance, and can be used to estimate the distance to an object [6]. The use of magnification is important to the advanced 3D reconstructions under investigation for this project [2].

There are two 'penalties' associated with coded-aperture imaging: First, unlike direct imaging where the uncertainty of a portion of the image is given by the uncertainty of the counts directly measured in that portion of the image, for coded-aperture imaging, the counts in the entire detector are used at each location of the image so that the uncertainty in each image pixel is given by the square root of the total number of counts used to make the image (with appropriate modifications for the weighting factors [7]). For large images decoded without oversampling, even though the same data are used over and over to create the image, no co-variance of uncertainties between image pixels exists. However, generally the images are created at twice their spatial resolution, e.g. oversampled a factor of two in each dimension (to minimize perceived source intensity changes with location) [8] and for such images there is a covariance term for neighboring pixels that must be considered [9, 7].

The second 'penalty' is that the scene is encoded as spatial variations in counts across the face of the detector and invariably, in addition to the desired count-rate variations due to the mask, there are undesirable variations due to background gradients, and detector non-linearities.[2] Fortunately the latter can be easily removed by using a mask/anti-mask technique [10] where the data are collected in two equal-time integrations; one with the mask and one with its inverse, or anti-mask, where the open and

[2] The mask/anti-mask technique also corrects for first order solid angle variations to different regions of the image plane [5].

closed holes have been exchanged. The sum of the two data sets will have no modulation due to the mask and can therefore be subtracted from the overall image. In fact, because the mask function for the anti-mask is simply the negative of the mask's mask function, the reconstruction can be performed in one operation using the mask function and a simple subtraction of the two data sets:

$$I_{i,j} = \sum_{m,n} M_{m-i,n-j}(D^{M}_{m,n} - D^{A}_{m,n}) \quad (4)$$

For this technique to work, the scene must remain constant during the two integrations and for this reason, the primary imaging target for the SPD application is during shift changes when there is no activity in the glove boxes. Those are expected to last 2 hours and should provide sufficient time to obtain images of even small quantities of Pu.

The mask/anti-mask technique is entirely automated by using modified uniformly redundant array (MURA) patterns [11] that are anti-symmetric on a 90^0 rotation about their center. In particular, the H420 standard pattern is a rank-19 MURA mask created by fitting 1.5-mm-thick tungsten pieces into a plastic printed holder and then potting the entire structure in epoxy.

Holdup Measurements

Conceptually, the advantages of the imaging approach under development to replace GGH, are simple. Specifically, one can see where material is located, and know that emissions from a given deposit are not contaminated by background radiation from other directions leaking through the GGH collimation. The potential accuracy of imaging has been previously demonstrated using a HPGe-based (high-purity germanium) coded-aperture imager to assay the amount of ^{235}U randomly distributed as oxide across 50 × 75 cm^2 GGH training cards used at the International Safeguards lab at ORNL. A simple point-and-click analysis of the images obtained from the data gave results within 3% of the known card values for multiple card configurations. Those results were based on extensive calibration of the imager used to collect the data, and were obtained with several emission line images, and uncertainties were validated using bootstrap sampling techniques [12, 13].

While the ^{235}U results show how imaging overcomes many of the systematic issues that plague GGH, further development is required before it can be applied at SPD. Specifically, the card data are for thin samples where self-attenuation and attenuation due to overlying equipment are not problems and with the material at a single fixed distance comprising a flat image plane. In the glove boxes, holdup will occur on and within process equipment that is at varying distances from the imagers. This means that depth-of-field issues will have to be addressed, as will attenuation due to potentially complex (and unresolved) lines of sight through the process equipment. We will also have to develop techniques to handle and determine the amount of self-attenuation in the plutonium oxide. We note that these issues are also common to GGH but that the imaging has the inherent advantage that material location can be determined in 3D to aid in a full modelling-based analysis that includes known structure and locations of process equipment. For these reasons, multiple imagers with overlapping fields of view will be installed on each glove box so that in some regions stereo imaging can be used to resolve the distance to holdup. Data using both the Compton and coded-aperture imaging modalities will also be used. The former will be particularly important at the top of the glove box where single or no coverage is obtained from the coded-aperture imaging.

To determine holdup we will take advantage of the same 129-keV line used in current GGH assays, but will also turn to the 375- and 414-keV lines to provide sensitivity to material in thick deposits and or material that is shielded by process equipment.

As mentioned, images will be available for any times when material is stationary during the mask/anti-mask integration intervals and those are expected be ~ 2 hours long and to occur twice daily. During some of these intervals we expect to have little or no in-process material in the glove box, allowing us to generate hold-up maps, while at other times in-process material will dominate allowing us to provide dose information for the next shift, and to look for material in anomalous locations. To

provide such information in a timely manner means that automated analysis techniques will have to be developed and are discussed in the companion paper [2].

H420 Imager

To collect imaging holdup data we plan to use a modified version of the H420, CZT-based, gamma-ray imager [14]. The commercial version of the instrument includes a detector plane comprising four 2.2 × 2.2 × 1 cm^3 CZT crystals with the 1.5 mm thick tungsten mask described above. The detector anode is subdivided into an 11 × 11 pixel array with each pixel read out independently. Interaction locations are determined parallel to the 2.2 × 2.2 cm^2 face of each crystal by identifying the pixel that collects the charge and then using transient charge signals observed by the neighboring pixels to interpolate the result to ~ 0.5 mm. The position in depth is determined with a similar accuracy by using a combination of the drift time as electron drift induces charge on the two detector faces and by using the ratio of the induced signal sizes. The energy resolution of the detector is better than 1% FWHM at 662 keV, a result achieved by using the event's known location within the crystal to compensate for charge losses. The crystals are separated by a 0.5 mm gap where no gamma-rays are recorded. The size of this sensitivity gap is increased by a 0.5 mm guard ring at the edge of the detector.

The instrument is sensitive to both single-site, and multiple simultaneous energy depositions, allowing it to serve as the focal plane of the coded-aperture imager and as a Compton camera. The former has a mask pixel pitch of 2.15 mm with a ~ 2.3 mm focal length (distance from the back of the mask to the front of the crystal) providing an angular resolution of ~ 5°, while in Compton mode the resolution is ~ 15°.

Modifications for use at the SPD glove boxes will include small changes to the instrument's outer dimensions so that it fits within the footprint allowed for the light fixture in the SPD design, removal of the internal batteries, and primary analysis moved from the imager to centralized computers with data streamed on hard-wired ethernet connections. We will also explore the design of the coded-aperture imaging system, specifically, in addition to the mask changes discussed below, conduct a trade study of the imager's resolution versus its field of view (varied by changing the spacing between the coded-aperture mask and the detector) to optimize the response for the planned 3D iterative reconstruction.

Coded-Aperture Imager Sensitivity

To allow quantitative holdup measurements the sensitivity of the coded-aperture imager must be known, and we are using the same approach used to successfully develop the HPGe system. The sensitivity of the imager across its field of view is determined by scanning sources of known strength over a regular array of points that somewhat over scan the primary field of view. At each of the measurement locations data are collected long enough to obtain good counting statistics in the spectral line of interest (typically better than 1%). The data are saved by the imager as list-mode data files, one for each measurement location.

Once the data are collected, they are analyzed using an automated routine. The H420 saves two types of files, one with binary event data including a timestamp, the livetime since the last event, the event energy, and its spatial location, and a second file that records time-stamped mask events. The latter indicate the time of the event, whether the mask is stationary or rotating and if stationary, whether it is in a mask or anti-mask orientation. On playback the mask information is used to segregate the event data into separate mask and anti-mask data cubes. Each data cube comprises a 2D array of the event distributions with one array for each of the 4096 energy bins. The pitch of the 2D binning is set to oversample the magnified mask pattern at the detector (based on the known distance to the source plane) by a factor of two. The livetimes for the mask and anti-mask data are individually integrated on an event-by-event basis for all events that occur during stationary mask positions. When a single source location's

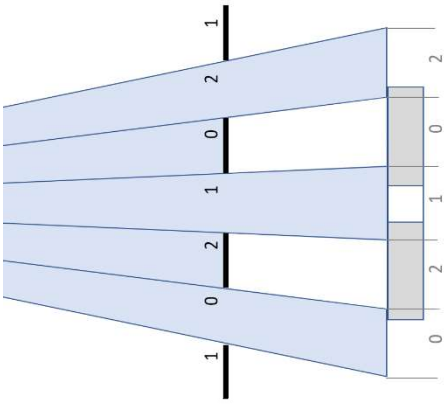

Fig. 1. Schematic showing how a repeated mask (black) encodes a shadow on the detector (gray) of diverging radiation (blue) emanating from a point source in the near field (off to the left). Mask pixels 0, 1, and 2 are sampled ~ 1.2, 0.5 and 1.0 times for weighting terms of 0.83, 2.0, and 1.0, respectively.

data have been integrated, the mask/anti-mask livetimes are used to determine a normalization factor for the longer (mask or anti) data set.

The data are then inverted using an eventimage structure that is described in detail in [7]. In short, the eventimage is generated by dropping a single event into each of the available detector bins and creating the cross-correlated image using (4) with that single datum. Nominally this would be a phase-shifted portion of the mask pattern with values of ± 1. However, because the detector can be larger than the projected mask pattern, and the mask is made of a 4-fold mosaic of the base pattern, some mask locations may be sampled more than once (Fig. 1) and events in each bin sampling the same location are weighted so that over the whole detector, each mask element is sampled uniformly. However, weighting factors also account for the relative fractional area of sampled mask elements (Fig. 1) that occur at the edges of the detectors, particularly for detector locations that occur in the gap between crystals. Such pixels may have individual event contributions larger than ± 1 based on the fractional overlap of area of the ideal detector bin with the actual detector area instrumented. To generate the contribution to the image from a given detector location, for each energy, the eventimage for that location is multiplied by the difference of the appropriately livetime-normalized mask and anti-mask events in a single detector datacube bin and then added to the composite image created from the other, similarly treated detector values from that energy. The result is a hyperspectral image (Fig. 2), with an image for each energy or conversely a full spectrum for each pixel of the image. For the analysis, a composite image based on the spectral region of interest (sROI) is then made by adding the images in the appropriate datacube spectral bins.

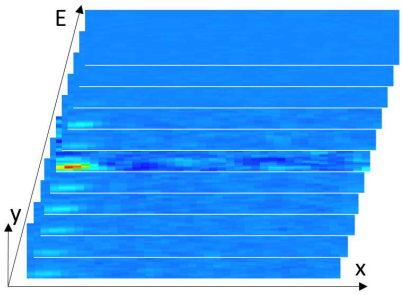

Fig. 2. Portion of a hyperspectral image datacube from 100 to 150 keV in 5 keV steps of a ^{57}Co source in the bottom left corner of the image. The spectral layers are slightly offset for clarity.

The resulting image is automatically scanned for the peak pixel and an 11×11 tile used as an area region of interest (aROI, Fig. 3). That aROI is first used to set the offset in the image [7] and then the counts in the aROI are summed to obtain the imager response at that location. When the analysis is complete there is a response for each of the scan locations and these can be plotted as false-color heat maps to indicate the instrument sensitivity (Fig. 4). These data can then be used to correct the observed intensity of a source to the actual emission strength at the image plane.

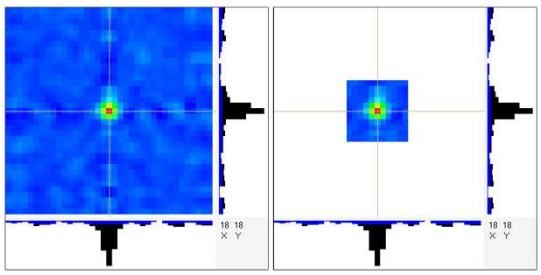

Fig. 3. False-color calibration image of a source at the center of the field of view (left), and the aROI (right). The histograms to the right and below the images show the counts under the cursor lines.

Unfortunately, due to many factors that change with energy, including the detector response function, the mask transparency, and the effective focal length, the sensitivity maps will be energy dependent (Fig. 4). In principle, one could perform source scans at regular energy intervals and then use interpolation to determine the response at other energies. In practice, suitable isotopic emission lines do not exist to create such a data set, so the goal of the source calibrations is to use them to validate Monte Carlo simulations at several energies and then run the Monte Carlo models with source locations similarly stepped across

the field of view at regular energy intervals to generate the sensitivity data cube needed to perform arbitrary corrections. The model is also important because it forms the basic input to more advanced iterative reconstruction approaches such as maximum likelihood expectation maximization.

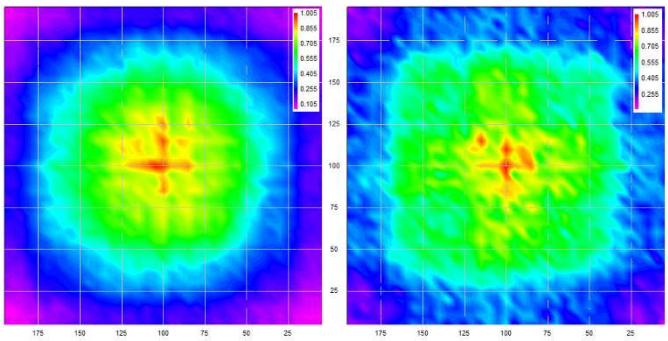

Fig. 4. False color sensitivity maps created at 81 keV (left) and 356 keV (right) using the phase-shifted, 3-mm-thick mask (see mask modifications section).

Monte Carlo Model

Simulated data for the H420 imager is generated via a multistep process involving radiation and particle tracking, event building, and application of a detector response model. The GEANT4 [15] physics simulation package handles both the propagation of gamma rays from a source to the imager and the tracking of energy depositions within the CZT crystal. A combination of detailed CAD drawings provided by H3D and in-lab measurements of interior imager components inform the GEANT4 geometry model. Inclusion of all relevant features in the forward field of view provides proper accounting of the effects from intervening material and potential scattering sites within the imager. The GEANT4 output consists of lists of energy depositions for all gammas interacting in the CZT. The depositions for individual gammas are then grouped into single detector events (or multiple events for gammas which interact in two or more non-neighboring pixels) which feature a single energy and location.

In order to more accurately reflect the detector performance, positional and energy smearing is applied to the simulated events. The energy smearing model utilizes the Doniach-Sunjic [16] asymmetric peak shape to produce probability density functions for energies spanning the range of interest at intervals of 1 keV with parameters provided by LBNL for related work in Compton imaging [17]. Comparison with measurement data (Fig. 5) shows that at low energies the fit is imperfect. Improvement is possible, but is adequate for current development work.

Multiple positional smearing models have been explored for use in the simulation package and development is continuing. Previous models made use of a truncated Gaussian distribution to smear event locations without pushing them outside of the detector pixel in which they reside. To reflect the observed degrading resolution toward crystal edges, the width of this Gaussian was increased for boundary detector pixels. However, flat-field and slit-scan calibration data sets revealed systematic biases in position reconstruction – predominantly manifesting in pixels along the crystal edges.

This motivated the creation of a new position response model that emulates the sub-pixel position determination algorithm used by the imager. This is done by calculating an induced signal on neighboring pixels proportional to the distance between that pixel and the true hit location. Smearing is applied to these signals which are then used to calculate a new event position. The systematic behavior of edge pixels is handled via parameterization of the smearing function. Optimal parameters for each crystal edge are determined by applying the response model to a flat event distribution and comparing the output to the

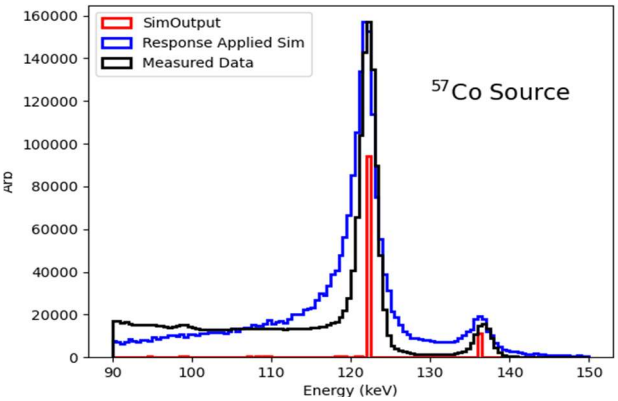

Fig. 5. Comparison of data, to the original and smeared (using 662 keV parameters) simulation output.

observed lab data. The result is a set of parameters for each edge pixel which can be fed into the position response model that visually matches data (Fig. 6).

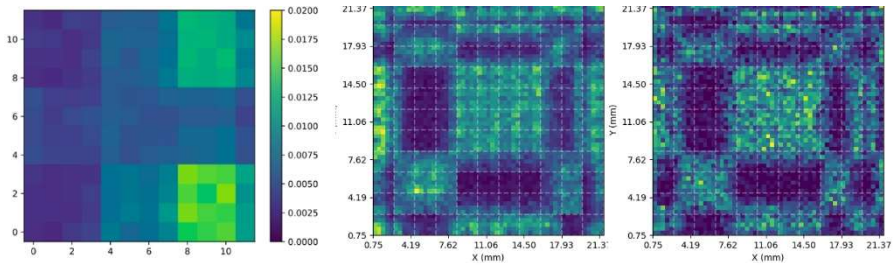

Fig. 6. Left, Event distribution within a sample edge pixel at 80 keV. Center, Portion of a measured shadowgram at 81 keV. Right, Portion of a simulated shadowgrom at 81 keV.

Simulation Performance

While the simulated and measured shadowgrams seem to match fairly well, a quick comparison of sensitivity maps created from them are found to differ significantly (Fig. 7). In particular, the data-based sensitivity maps fall off more rapidly towards the corners of the field of view than do the simulation maps. Overall, we are confident that the GEANT4 code is not at fault and that the mechanical model is largely correct based on a comparison of the *non-imaged* response maps (Fig. 8). These maps show the number of events seen by the detector at each source location and match the data much better than the imaging response maps at the energies where they have been compared. Because a similar fall off in sensitivity at the corners of the response map is observed in scans of several detectors, at several energies (81 keV and 122 keV), and with the alternate mask configurations (see below), we are confident that these are not due to aberrations in the spatial response of the crystals in a single detector.

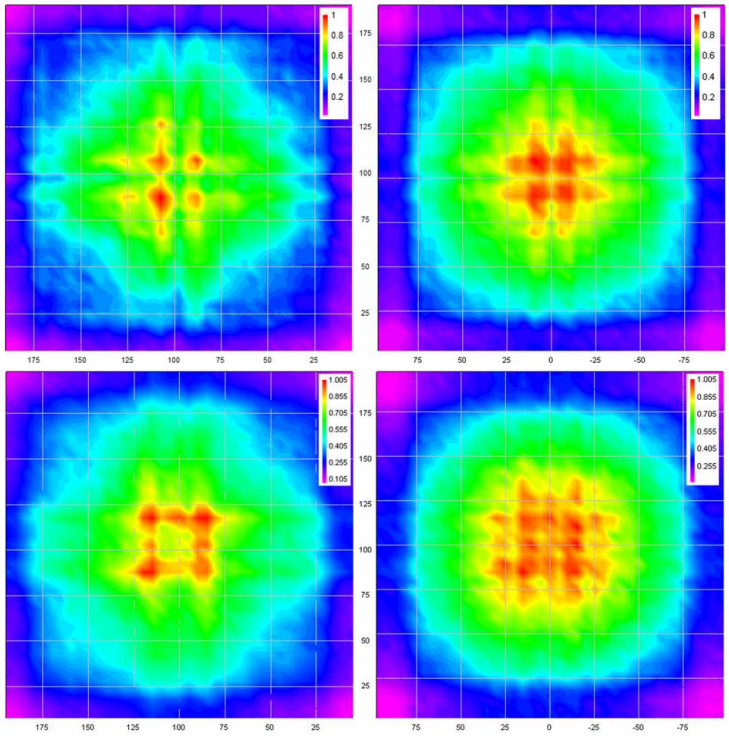

Fig. 7. Comparison of data (left) and simulation (right) sensitivity maps with the original mask at 81 keV (top row) and the all-metal, phase-shifted mask at 122 keV (bottom row).

The current working theory is that the discrepancies are linked to errors in processing the Monte Carlo energy depositions into their corresponding blurred events, particularly near the edge of the detector. For some of the shadowgram data we have noted different behavior between the inside (edge adjacent to another crystal) and outside crystal edges with the latter showing the expected decrease in contrast, while the former shows less degradation and evidence that the pattern is displaced in the edge direction. The asymmetric performance could be explained by the electric field cage provided by the neighboring CZT crystals. The situation is complicated by the presence

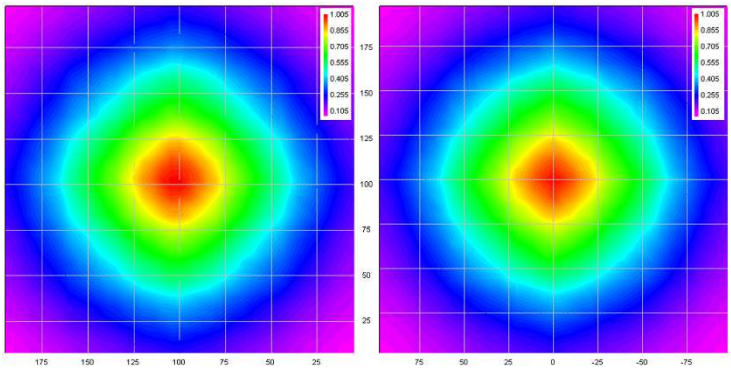

Fig. 8. Sensitivity maps for total counts in the 121-keV line for data (left) and simulations (right) with the 3-mm-thick, phase-shifted, all-metal mask. The two are very similar.

of a guard ring and how charge from under that ring is handled. If it is pulled toward the pixelated portion of the detector, that could appear as a shift in the recorded shadowgram. To explore this, data from the edge pixels have been excluded from the analysis in both the data and simulation, and there is less difference between those two sensitivity maps. Unfortunately, this could be also be due to the incomplete mask sampling dominating other aberrations in the image formation.

In exploring this further, we have probed the local response function of the CZT detectors by removing the mask and exposing them with radiation through multiple parallel 500 μm slits oriented both horizontally and vertically. The slits are separated by ~ 8 mm and data were collected at locations stepped by 380 μm to fully scan the crystal array. The results clearly show some localized displacement to the events (Fig. 9) that vary from crystal to crystal. However, since the overall imaged response of different imagers is similar, these are not considered important. A detailed analysis of the edge regions is in progress.

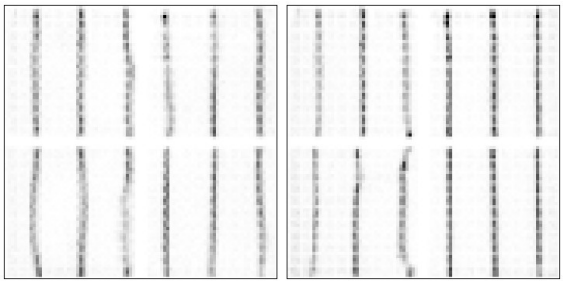

Fig. 9. Slit scan data for two different detector arrays. The inter-crystal gap is clearly visible halfway up the images. Localized event shifts show up as curvature to the lines.

Mask modifications

Data have been collected with the standard mask described above, and with modified masks designed to improve the overall performance of the imager. The first modification is to replace the 1.5 mm thick W mask with one that is 3 mm thick. This has little effect at 129 keV, but decreases the mask leakage at the 375- and 414-keV lines from 0.56 and 0.62, to 0.31 and 0.38, respectively, increasing the imaging efficiency. We expect to use these lines in situations where the brighter 129-keV line is attenuated either through self-attenuation in thick deposits or due to overlying portions of the process equipment. In fact, if we can obtain sufficient statistics at both 129 keV and ~ 400 keV, then we can perform gamma-gauging to help determine attenuation corrections for the amount of holdup present.

As part of the effort to understand the roll-off in sensitivity towards the corners of the fields of view we have also had all-metal masks made out of single W sheets. This provides a more precise pattern and has the additional benefit of removing the potting material in the 'open' mask elements. This increased transmission through those elements and improved the imaged source intensity at 122 keV by 11%.

Finally, we changed the phase of the mask to move the completely open and closed row and column of the pattern away from the center of the standard rank-19 MURA mask design (Fig. 10, left). This was done to remove the interaction of those mask elements with the dead band between the crystals in the detector plane. Specifically, as a source shifts from the center of the field of view the shadow of those mask elements falls from the partially missing pixels to fully instrumented regions of the detector plane. Any errors in the scaling of the data to compensate for the missing detector area will be worse for the completely open and closed rows as compared to the standard rows and columns which are 50% open or closed. This did improve the flatness of the response maps for the redesigned masks (Fig. 10.)

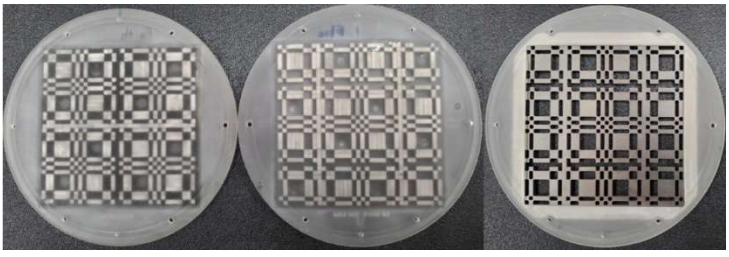

Fig. 10. From left to right, original H420 mask, revised-phase mask, and revised-phase, 3-mm-thick, all-metal mask.

Path Forward

While we continue to explore the discrepancy between the simulated and laboratory data, we are also developing correction algorithms that allow for simple point-and-click analysis of the amount of Pu in

the field of view. Regardless of the source of an efficiency map (data or simulation) it must be applied to the images to flatten the response function. In the prior work with the HPGe imager, simple inversion and correction on a pixel-by-pixel basis was found to result in systematic errors when the data used to generate the maps were subsequently analyzed using the corrections. This was traced to an interaction between the distributed point spread function (PSF, which is spread over several pixels) and the pixel-by-pixel correction map. That is particularly important for the H420 imager where there are high-frequency spatial changes to the response. Corrections made to data from one pixel blurred to a neighboring pixel by the PSF will be improperly corrected. For a slowly varying sensitivity this will only create small errors that tend to average out with overcorrections made to pixels on one side of the center, compensated by undercorrections made on the other side, e.g. for a slowly varying correction map. However, if there are more rapid changes then the pixels on opposite sides of the distribution will be over- and under-corrected by different amounts.

To compensate for such effects, we generate the correction maps in a two-step process. First the map is simply inverted and used to create a pixel-by-pixel correction map, $C_{i,j}$. The data used to create the map are then replayed using the correction map to create a new sensitivity map, $Q_{i,j}$, that shows where the counts are over and under corrected. This map is then used to scale the original correction map using a weighting fraction based on how much the originally corrected map deviates from the average pixel value, Q_{avg}:

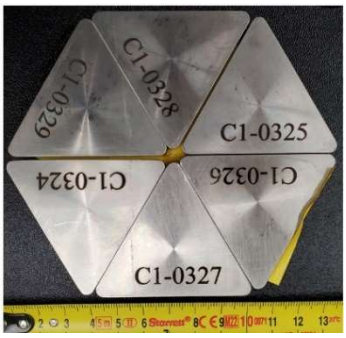

Fig. 11. Six triangular ^{239}Pu sources each with ~ 1.8 g of Pu.

$$Z_{i,j} = C_{i,j}\left(1 + f\frac{Q_{i,j} - Q_{avg}}{Q_{avg}}\right) \quad (5)$$

The original imaged data are then reanalyzed using correction maps with a range of f values and the one with the flattest response used as the final result. To determine the flatness, the outer five rows and columns of the response map are removed (because they contain wrapped source locations) and the sigma value of the fluctuation of the remaining pixels about the average pixel value calculated. For the ^{57}Co data the minimum sigma is 4.6% (f=0.7), which is ~ 3 times worse than that obtained with the HPGe system and is attributed to the high spatial frequency changes in efficiency as a function of location, but represents a good starting point against which to compare other approaches.

While a full correction cube spanning the detector energy range requires fixing the simulation response, the 122-keV line from ^{57}Co is sufficiently close to the 129-keV emission line planned for conducting much of the SPD holdup assay, that it can be used without corrections due to the energy. This has been tested by applying it to data collected with ^{239}Pu. Six triangular sources [18] (Fig. 11) each containing ~ 1.8 g of ^{239}Pu attached to the same translation stage used to collect the calibration data and moved across a 12 × 12 grid spanning 100 cm in each axis. The data were then analyzed as point sources (the hex array is comparable to a resolution element) with a pixel-by-pixel intensity correction applied using the ^{57}Co correction maps. The resulting intensity map (Fig. 13) has a 4.6 %, 1-sigma deviation about the average.

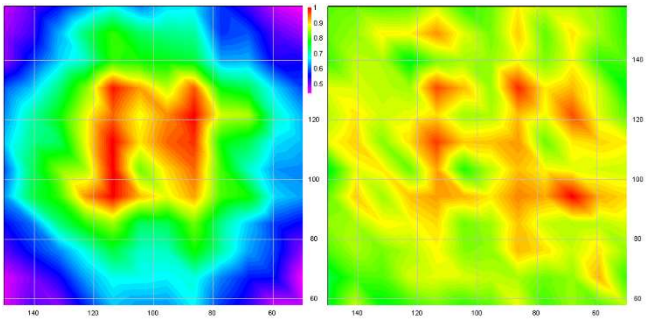
Fig. 12. Sensitivity map for Pu (left), and corrected and normalized activity result (right). Both plots use the same color scale.

Conclusion

The H420 imager from H3D Inc. is being studied as a tool to perform regular holdup monitoring of glove boxes that will be used to process surplus Pu for permanent disposal. A new mask design has been tested that improves the sensitivity for both the129-keV and the ~ 400-keV ^{239}Pu spectral emissions. These will be used to generate quantitative images during the multiple daily shift changes when the radiation environment of the glove boxes is static. When no material is in process, such images will provide quantitative holdup measurements replacing the more labor-intensive manual GGH measurements currently planned, and without requiring additional down time to perform the measurements. When process material is present, the images will provide timely radiation maps to aid in minimizing dose to workers. Imager calibration with various radioactive sources have been performed and we are currently working to improve the fidelity of simulations so that general-purpose correction cubes can be generated across the instruments spectral range.

References

1. K. Schmitt, et al. this proceedings.
2. A. Laminack, et al. this proceedings.
3. R.H. Dicke, *Astrophys*. J., **153**, L101, 1968
4. E.E. Fenimore, T.M. Canon, *Applied Optics*, **17**, 337, 1978.
5. R. Accorsi, R. Lanza, *Applied Optics*, **40**, 4697, 2001.
6. J. Braverman, et al. *IEEE Trans. Nucl. Sci.*, **62**, 1405, 2015.
7. K.P. Ziock, M.A. Blackston, *Nucl. Inst. Meth.in Phys. Res.*, **A916**, 56, 2019.
8. E. Caroli, et al., Space Sci. Rev., **45,** 349, 1987, 349.
9. M.C. Fleenor, M.A. Blackston, K.P. Ziock, *Nuc. Inst. Meth. in Phys. Res.*, **A784**, 370, 2015.
10. J. Braga, et al., *Exp. Astron.*, **2**, 101, 1991.
11. S.R. Gottesman, E.E. Fenimore, *Applied Optics*, **28**, 4344, 1989.
12. K.P. Ziock., et al., Proc. INMM & ESARDA Joint Ann. Meeting, (Virtual) 2021.
13. K.P. Ziock, et al., Proc. of the IAEA Symp. on International Safeguards: Reflecting on the Past and Anticipating the Future, IAEA CN-303,Vienna, Austria, Nov. 2022.
14. H3D, Inc. 812 Avis Dr., Ann Arbor, MI 48108.
15. S. Agostinelli et al., *Nucl. Instr. Meth. in Phys. Res.*, **A506**, 250, 2003.
16. S. Doniach and M. Sunjic, *J. Phys. C: Solid State Phys.*, **3**, 285, 1970.
17. D. Hellfeld, et al., Proc. INMM 63rd Ann. Meeting, (virtual) 2022.
18. C. Blessinger, M. Dion, J. Garrison, in Proc. INMM 61st Ann. Meeting, Baltimore, MD, July 2020.